



Research articles

Superparamagnetic microbead transport induced by a magnetic field on large-area magnetic antidot arrays

Minae Ouk, Geoffrey S.D. Beach*

Department of Materials Science and Engineering, Massachusetts Institute of Technology, Cambridge, MA 02139, USA



ARTICLE INFO

Article history:

Received 21 April 2017

Received in revised form 29 July 2017

Accepted 30 July 2017

Available online 3 August 2017

ABSTRACT

A method is presented for directed transport of superparamagnetic microbeads (SPBs) on magnetic antidot patterned substrates by applying a rotating elliptical magnetic field. We find a critical frequency for transport, beyond which the bead dynamics transitions from stepwise locomotion to local oscillation. We also find that the out-of-plane (H_{OOP}) and in-plane (H_{IP}) field magnitudes play crucial roles in triggering bead motion. Namely, we find threshold values in H_{OOP} and H_{IP} that depend on bead size, which can be used to independently and remotely address specific bead populations in a multi-bead mixture. These behaviors are explained in terms of the dynamic potential energy landscapes computed from micromagnetic simulations of the substrate magnetization configuration. Finally, we show that large-area magnetic patterns suitable for particle transport and sorting can be fabricated through a self-assembly lithography technique, which provides a simple, cost-effective means to integrate magnetic actuation into microfluidic systems.

© 2017 Elsevier B.V. All rights reserved.

1. Introduction

Controlling the motion of small particles using magnetic fields can provide a simple means for directed transport in lab-on-a-chip applications [1–4], while enabling useful functionalities such as sorting of biological materials. Chip-based magnetic actuation mechanisms are usually based on discrete permanent magnets or electromagnets positioned near micro-channels, where surface-functionalized superparamagnetic microbeads (SPBs) can be influenced using magnetic field gradients [5–13]. However, uniform particle motion over long distances is not possible using externally placed magnets due to the inverse-cube dipole field profile that leads to a nonlinear position dependence of the force profile, and in the case of localized microelectromagnet arrays, heating can be a serious problem [9,14]. Therefore, much research has focused on alternative means for controlling colloidal particles [15–28], especially with high precision [29]. A promising approach is the use of micropatterned magnetic substrates that lead to a periodic local stray field profile that can be modulated using an external magnetic drive field. By using periodic driving fields, magnetostatic interactions between SPBs and the substrate can lead to a dynamic magnetic potential energy surface in which local energy wells propagate uniformly across a surface. This can be used to induce magnetic particle transport [30,31] and other dynamical behavior

[32,33] that can be utilized to achieve functionalities such as particle separation and sorting [16,30,34–36]. In particular, by tuning the frequency or phase difference between the orthogonal field components in a rotating field configuration, it has been shown that “ratcheting” behavior can be used for multiplexing of polydisperse mixtures of magnetic beads transported across a substrate. This was achieved using a square lattice of circular soft magnetic dots whose magnetization profiles are controlled by the external field [32]. Given the complexity of the interactions, one might anticipate that there may also be other factors that can control the dynamics and could be utilized in multiplexed sorting operations.

In this work, we examine the dynamics of SPBs driven across magnetic antidot arrays [37–42] by a rotating out-of-plane elliptical magnetic field. We find not only a critical frequency for transport, but also threshold field values demarking the transition between bead motion and local oscillation, and that the latter allows for individually addressing magnetic beads with particular characteristics in a mixture. These thresholds provide a new, simple control parameter for highly selective sorting which can be used in conjunction with a two-dimensional periodically-patterned substrate for transport and separation of individual populations of beads interspersed on the same chip. Micromagnetic simulations are used to calculate the stray field profiles and potential energy landscape, in order to explain the observed behavior and to understand the impact of the relation between the bead size and substrate periodicity. Finally, we show that a simple

* Corresponding author.

E-mail address: gbeach@mit.edu (G.S.D. Beach).

floating-transfer technique can be used to fabricate large-area self-assembled hexagonal arrays of polystyrene microspheres that serve as a lithographic mask to prepare antidot arrays suitable for SPB transport. Compared to other approaches for the integration of magnetic patterns in lab-on-a-chip systems, such as optical lithography on flexible membranes [43] or electron-beam lithography with water based lift-off [44], self-assembled lithography provides a simple and cost-effective method with minimal lithographic processing. These results demonstrate the possibility to incorporate simple, low-cost magnetic actuation into microfluidic chip-based platforms to augment or replace conventional actuation mechanisms.

2. Experimental methods

We examined dependence of field-driven microbead transport (Fig. 1(a)) on symmetry and transport direction using antidot arrays fabricated by optical lithography. Antidot arrays with square

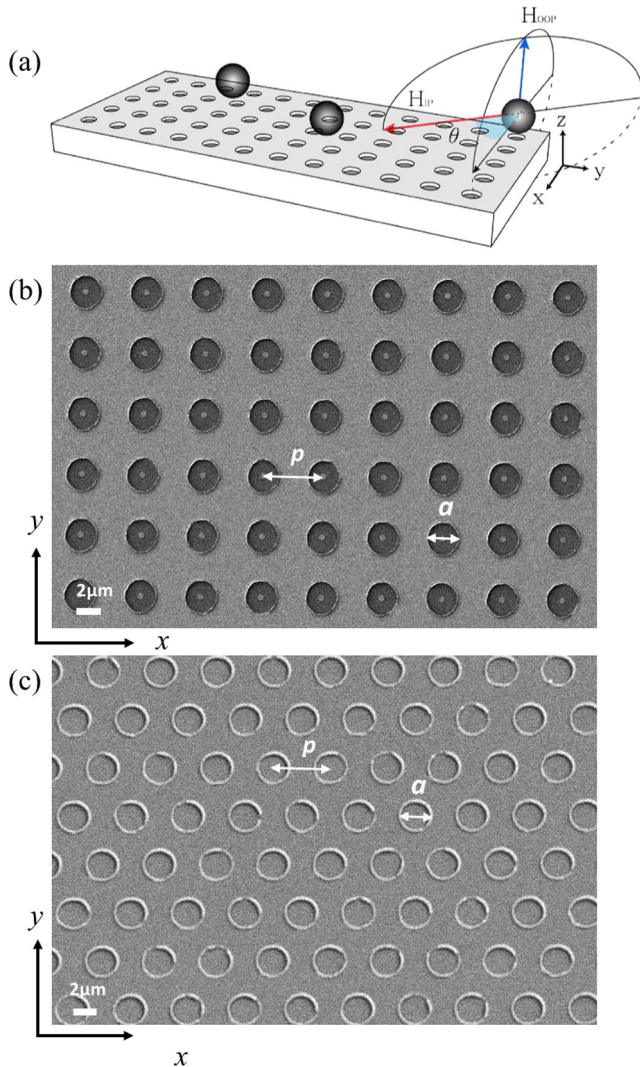


Fig. 1. (a) Schematic of the superparamagnetic bead motion experiments. The blue arrow represents the amplitude of the out-of-plane field H_{OOP} and the red arrow shows the amplitude of the in-plane field H_{IP} . θ is the angle between the H_{IP} component and the x -axis. (b),(c) Scanning electron micrograph images of Co antidot arrays with square lattice symmetry (b) and hexagonal lattice symmetry (c). p is the periodicity of the pattern and a is the average diameter of the antidots. (For interpretation of the references to colour in this figure legend, the reader is referred to the web version of this article.)

and hexagonal symmetry, and center-to-center nearest neighbor spacing p , were patterned onto thermally-oxidized Si(100) wafers using a standard lift-off technique. The shape of the antidots was chosen to be circular to ensure that the holes themselves did not contribute to the anisotropy of the antidot array [45]. After resist exposure and chemical development, a 40 nm thick Co layer was deposited by DC magnetron sputtering at room temperature at an Ar pressure of 3.0 mTorr. The Co layer thickness was chosen to be thick enough to produce significant magnetostatic stray fields [23], without being so thick as to induce topographical texture that could inhibit bead movement. Following liftoff, the wafer was coated with a 70 nm thick protective SiO_2 layer, chosen to be thick enough to coat the sidewalls of the Co pattern, while thin enough to maintain a close distance between magnetic beads and the underlying Co film [30]. Prior to experiments, the substrate was cleaned in isopropyl alcohol followed by several rinsing steps in de-ionized water, and in some cases a peroxide passivation step. In addition, the beads were suspended in a phosphate-buffered saline (PBS), in some cases with 0.1% (v/v) Tween 20 detergent, in order to minimize surface adhesion between beads and substrate.

Fig. 1(b) and (c) show scanning electron micrographs of Co antidot arrays with $p = 5 \mu\text{m}$ and hole diameter of $2.5 \mu\text{m}$ with a square and hexagonal lattice symmetry, respectively. Vibrating sample magnetometry was used to characterize hysteresis loops of the patterned films; we find relatively square loops with a coercivity $\mu_0 H_c \sim 6 \text{ mT}$, with only weakly anisotropic behavior in the plane.

Bead motion experiments were performed using commercially available SPB microbeads with several diameters: Dynabeads M270 Carboxylic Acid ($2.8 \mu\text{m}$ diameter) from ThermoFisher (catalog number 14305 D), carboxyl magnetic $4.3 \mu\text{m}$ beads from Spherotech Inc. (catalog number CM4010), and COOH modified beads ($5.8 \mu\text{m}$ diameter) from Bangs Laboratories (catalog number UMC3 N). The magnetic susceptibility has been previously reported to be $\chi \approx 0.17$ for the $2.8 \mu\text{m}$ [46] and $5.8 \mu\text{m}$ [47] beads. Dilute bead suspensions were placed in a polydimethylsiloxane (PDMS) well on the wafer, and then sealed with a microscope cover slip. These samples were placed on a customized electromagnet that was composed of an out-of-plane field air coil and an in-plane field quadrupole magnet for applying the magnetic field. The magnet, powered by two different power amplifiers, can generate an in-plane field ($\mu_0 H_{IP}$) of up to $\sim 50 \text{ mT}$ and out-of-plane field ($\mu_0 H_{OOP}$) of up to $\sim 40 \text{ mT}$, respectively. We applied rotating out-of-plane elliptical magnetic fields with frequency f , rotating in a plane oriented at an angle θ with respect to the lattice principle axis (see Fig. 1(a)). The time-dependent field components are given by $H_{IP}(t) = H_{IP} \sin(2\pi ft)$ and $H_{OOP}(t) = H_{OOP} \cos(2\pi ft)$, H_{IP} and H_{OOP} are the in-plane and out-of-plane field amplitudes, respectively. The range of frequencies used in bead experiments was from 0.25 Hz to 20 Hz or 30 Hz for $2.8 \mu\text{m}$ SPBs and $4.3 \mu\text{m}$ SPBs, respectively. Bead motion was observed using a home-built microscope integrated into the electromagnet stage setup.

3. Results and discussion

Before starting measurements, we applied a large H_{IP} , to saturate the film magnetization along the same direction as the in-plane component of the subsequent rotating magnetic field, hence initializing the domain pattern. A rotating field was then applied as described above, and the bead trajectories were tracked in real time using a camera affixed to the microscope. Fig. 2(a) and (b) show the average velocity v of SPBs as a function of f for bead diameter $d = 2.8 \mu\text{m}$ on the square lattice sample of Fig. 1(b), with the field rotating in the xz plane. Though the motion was more or less uniform for all beads in each experiment, surface adhesion causes a

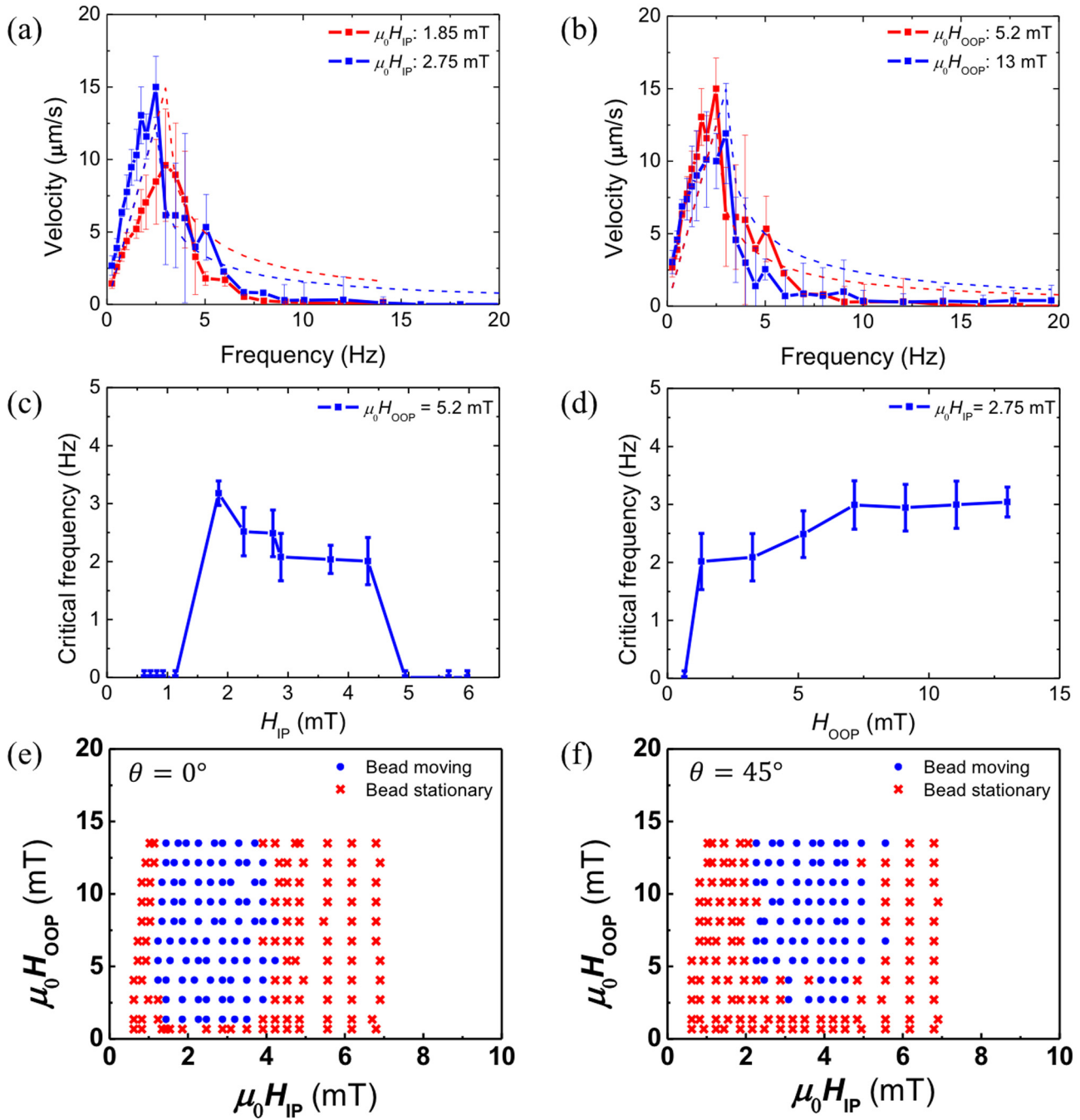


Fig. 2. Velocity as a function of frequency for SPB diameter of 2.8 μm at (a) $H_{OOP} = 5.2$ mT and $H_{IP} = 1.85$ mT, 2.75 mT. (b) $H_{OOP} = 5.2$ mT, 13 mT and $H_{IP} = 2.75$ mT. The dashed lines are the analytical model calculations the 2.8 μm. (c) The critical frequency as a function of H_{IP} under $H_{OOP} = 5.2$ mT for 2.8 μm diameter SPBs. (d) The critical frequency as a function of H_{OOP} at $H_{IP} = 2.75$ mT with 2.8 μm diameter of SPBs. Critical threshold of both H_{IP} and H_{OOP} for both (e) $\theta = 0^\circ$ and (f) $\theta = 45^\circ$. The blue dot means that we can observe the bead transport and the red cross means that SPBs just oscillate back and forth. (For interpretation of the references to colour in this figure legend, the reader is referred to the web version of this article.)

small fraction of beads to remain immobile; hence, we only consider measurements for those beads that have continuously moved for 10 s. Average velocities were obtained as the mean of the individual velocities of approximately 80–140 beads under each experimental condition. Fig. 2(a) shows mean v and standard deviation (plotted as an error bar) versus f at a fixed H_{OOP} and two different H_{IP} values, while Fig. 2(b) shows mean v versus f at fixed H_{IP} and two different H_{OOP} values. The results show similar behavior, with a linear increase of mean v with f up to a critical frequency f_c , followed by a dropoff, as also reported previously in periodically-patterned substrates [30]. This phenomenon could be explained

the fact that most of the beads cease to move (at least 80%) at higher drive frequency and only oscillate back and forth.

We analyzed the relationship between v and f , using a magnetophoretic transport model introduced previously [30,32,33]. The basic concept is that the rotating field causes a periodic rotation of the induced magnetization in the SPB, leading to a periodic potential landscape due to the magnetostatic interaction between the particles and the field gradients generated by the underlying substrate. In this model, the bead jumps from hole to hole along the pattern up to a critical frequency, beyond which the hydrodynamic drag begins to dominate and the bead position tends to

oscillate in a local spatially-oscillating potential well rather than jumping from one well to the next. The average velocity in this model can be described analytically by [30]:

$$v = \begin{cases} \omega \frac{p}{2\pi} & \text{for } \omega \leq \omega_c \\ (\omega - \sqrt{\omega^2 - \omega_c^2}) \frac{p}{2\pi} & \text{for } \omega > \omega_c \end{cases} \quad (1)$$

where p is the center-to-center distance between adjacent magnetic features (holes), and $\omega_c = 2\pi f_c$ is related to the ratio of magnetic force to viscous drag. In Eq. (1), v remains positive even for $\omega > \omega_c$, but its value decreases dramatically, and experimentally the SPBs are observed to be immobilized (oscillating about a fixed position) [30]. We fitted the experimental data with Eq. 1 (dashed curves) showing that this model describes the bead transport well.

From the fits, we extracted the critical frequency f_c , which corresponds to the peak in the average velocity versus frequency data. Fig. 2(c) and (d) show the dependence of f_c on H_{IP} for fixed H_{OOP} (Fig. 2(c)) and on H_{OOP} for fixed H_{IP} (Fig. 2(d)), for beads with $d = 2.8 \mu\text{m}$. It is found that there is a sharp threshold for the amplitude of both field components, below which the beads are immobile, and above which the beads can be transported. We note that f_c is independent of field amplitude above this threshold. However, there exists an upper threshold in H_{IP} , which occurs near the coercive field of the patterned film. This observation suggests that when H_{IP} exceeds this threshold, both the induced bead magnetization and the film magnetization (and resulting free pole configurations near the antidots) reverse sign together, so that the potential energy minima remain fixed in position rather than translating stepwise from one antidot edge to the next.

Fig. 2(e) and (f) map out the field parameter space in which bead motion is observed, using a rotating field frequency of 1 Hz, which is below f_c , and varying the in-plane and out-of-plane field components. Results are shown for the transport of $2.8 \mu\text{m}$ SPBs. A blue circle indicates that most of the SPBs could be transported in each magnetic field combination, whereas a red cross indicates that the beads oscillate back and forth locally rather than exhibiting stepwise translation. In addition, the working ranges or threshold values for both H_{IP} and H_{OOP} also significantly depend on the angle of H_{IP} when comparing Fig. 2(e) and (f), in which the rotating field plane and transport direction is along $\theta = 0^\circ$ and $\theta = 45^\circ$ with respect to the x-axis, respectively.

Next, we examine the dependence of f_c and the thresholds in both H_{IP} and H_{OOP} on SPB size and symmetry of the antidot pattern. Fig. 3 (a) shows v as a function of f at $H_{OOP} = 5.2 \text{ mT}$ and $H_{IP} = 1.85 \text{ mT}$ for three cases: $2.8 \mu\text{m}$ SPBs on the square anti-dot array, $2.8 \mu\text{m}$ SPBs on the hexagonal anti-dot array, and $4.3 \mu\text{m}$ SPBs on the square anti-dot array. The three curves are qualitatively similar; however, the dropoff in v above f_c is much less pronounced for the larger bead, whose diameter approaches the antidot lattice spacing, suggesting that another transport mechanism exists at higher frequencies, such as bead rolling [48–52]. The f_c of each case is 3.0 Hz , 2.0 Hz , and 2.5 Hz for $2.8 \mu\text{m}$ SPBs on square symmetry, $2.8 \mu\text{m}$ SPBs on hexagonal symmetry and $4.3 \mu\text{m}$ SPBs on square symmetry, respectively. Therefore, f_c has only a slight dependence on these parameters within the examined range.

Although f_c is rather weakly dependent on bead size, H_{IP} and H_{OOP} exhibit critical values that are more sensitive to bead and substrate parameters. Fig. 3(b) and (c) show the working ranges for the transport of $4.3 \mu\text{m}$ SPBs and of $2.8 \mu\text{m}$ SPBs as a function of magnetic field components: H_{IP} and H_{OOP} on the square anti-dot array and the hexagonal anti-dot array, respectively, at 1 Hz . Fig. 3(a), as well as a comparison of Fig. 2(e) and Fig. 3(c), show that the lattice symmetry does not significantly influence the f_c or the critical field values in the cases that the hole-to-hole spacings are

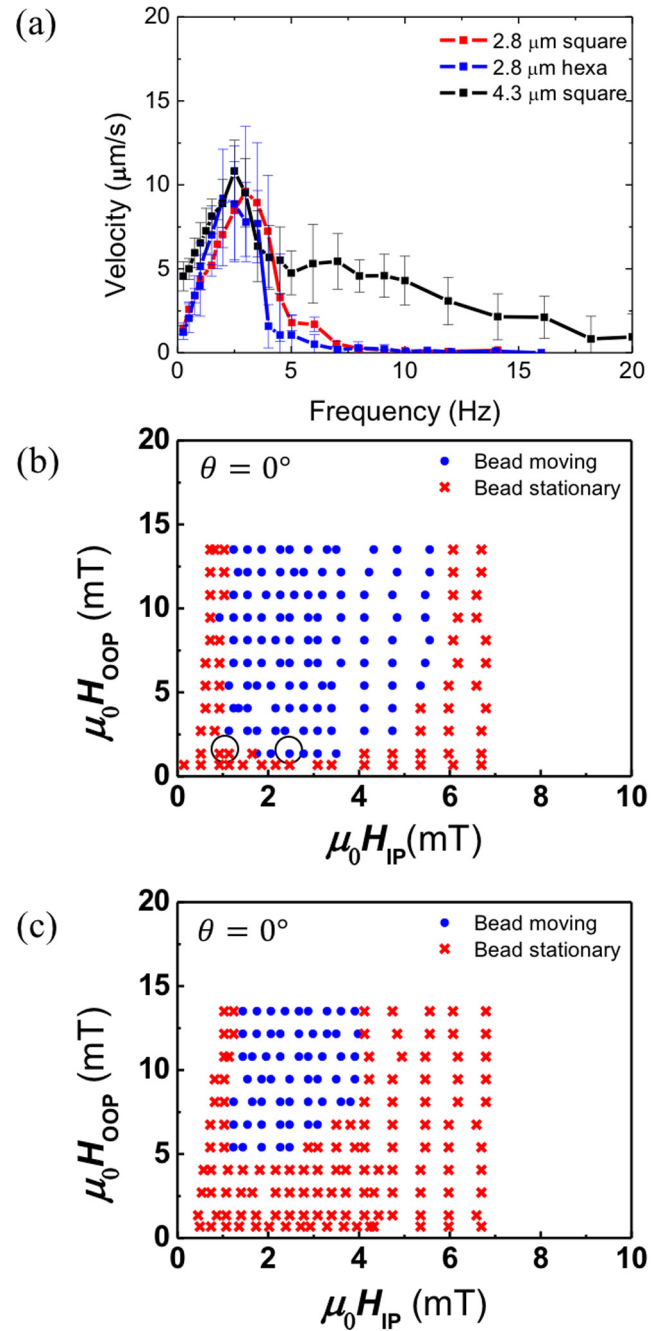


Fig. 3. (a) Velocity as a function of frequency at SPB diameter of $2.8 \mu\text{m}$ and $4.3 \mu\text{m}$ at $H_{OOP} = 5.2 \text{ mT}$ and $H_{IP} = 1.85 \text{ mT}$ on the square antidot array and on the hexagonal antidot array. Critical threshold of both H_{IP} and H_{OOP} for both (b) $4.3 \mu\text{m}$ diameter beads on the square antidot array that is magnetized along $\theta = 0^\circ$ and (c) $2.8 \mu\text{m}$ beads on the hexagonal antidot array that is magnetized along the $\theta = 0^\circ$ direction.

similar. By contrast, comparison between Fig. 2(e) and Fig. 3(b), which show the behavior for the $2.8 \mu\text{m}$ and $4.3 \mu\text{m}$ SPBs on the same square lattice, reveals a significant difference in the upper threshold for H_{IP} for different bead sizes. We expect this difference to be related to the different magnetic volume, possibly in conjunction with a different volume susceptibility due to different magnetic loading used by different manufacturers. When comparing Fig. 2(e) to Fig. 3(b) and (c), the transportation of $4.3 \mu\text{m}$ SPBs on the square anti-dot array are generally observed in a wider range of applied fields.

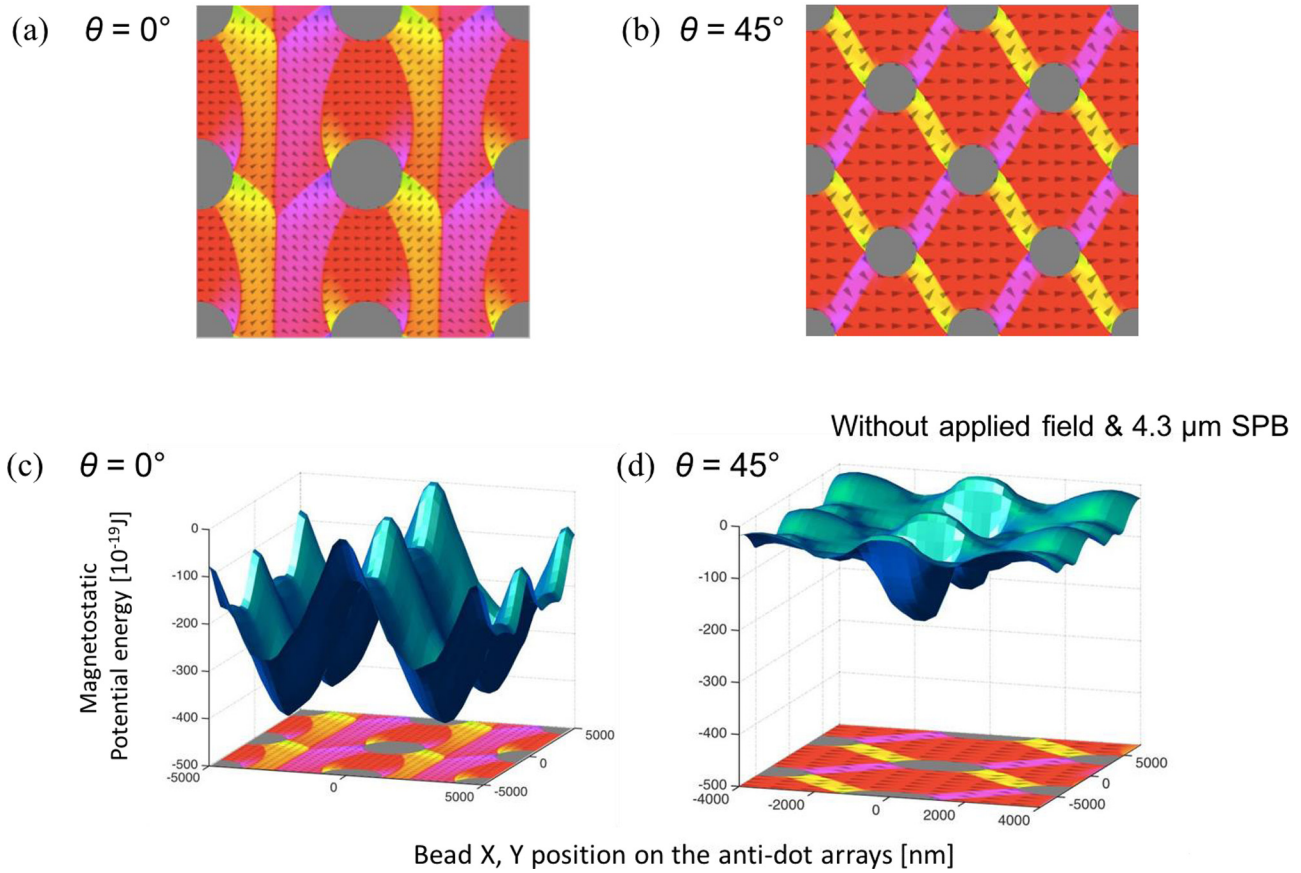


Fig. 4. The relaxed micromagnetically-computed magnetization configuration for (a) $\theta = 0^\circ$ and (b) $\theta = 0^\circ$ and magnetostatic potential energy landscape for (c) $\theta = 0^\circ$ and (b) $\theta = 45^\circ$.

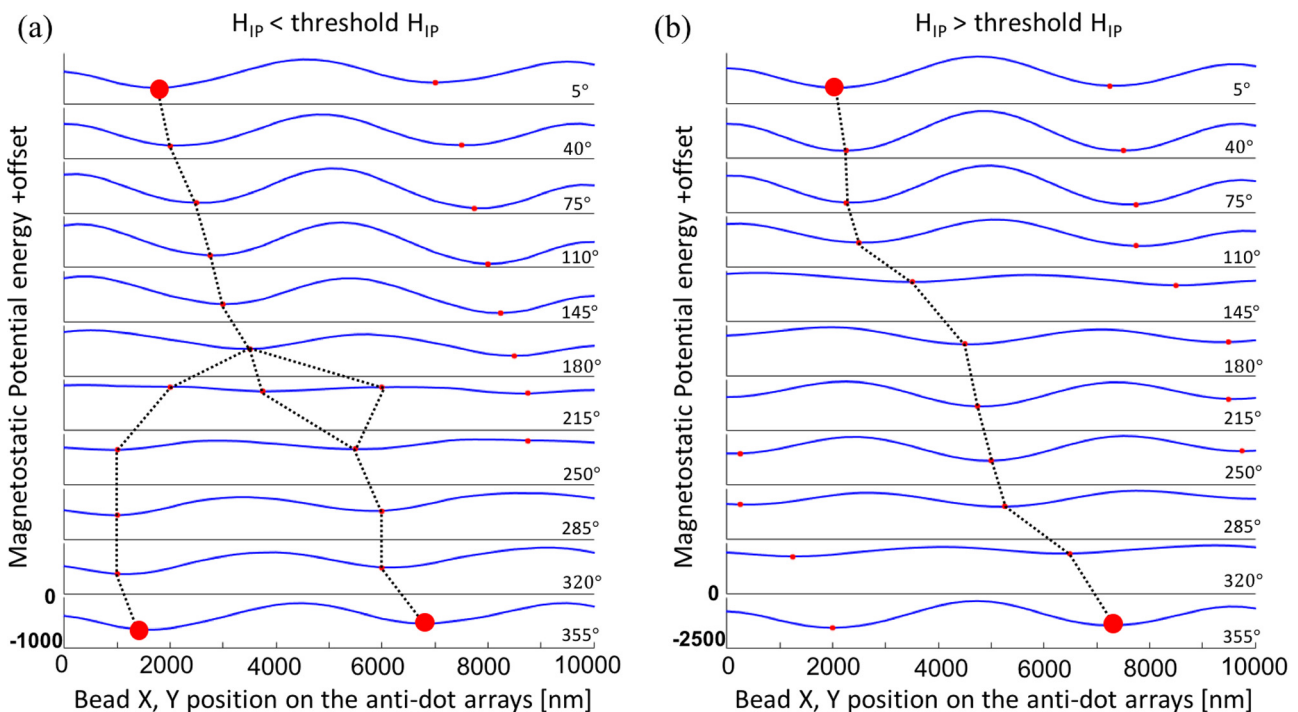


Fig. 5. The cross-sections of potential wells for 4.3 μm SPBs and minimum position (red circle) tracking at two different magnetic fields (a) the red area and (b) the blue area in Fig. 3 (b). (For interpretation of the references to colour in this figure legend, the reader is referred to the web version of this article.)

To understand the transport phenomena in more detail, we performed micromagnetic simulations of the magnetization patterns in the various cases, and computed magnetostatic potential landscapes as a function of field rotation angle and amplitude. In the micromagnetic simulations, the systems were divided into $4 \times 4 \times 40 \text{ nm}^3$ cells, and material parameters consistent with bulk Co were used: saturation magnetization $M_s = 1.4 \times 10^6 \text{ Am}^{-1}$, exchange stiffness constant $A = 3 \times 10^{-11} \text{ Jm}^{-1}$, and the magnetocrystalline anisotropy was set to zero because of the polycrystalline nature of the Co films. DW structures were calculated micromagnetically through the Mumax micromagnetic framework [53], and they were used as an input file to compute the stray field $\mathbf{B}(\mathbf{r})$ as a function of position \mathbf{r} . The magnetostatic potential energy of SPBs was approximated by integrating the dipolar energy density $-\mathbf{M} \cdot \mathbf{B}$ over the bead volume. In this step, we assumed that the bead magnetization $\mathbf{M} = \chi \mathbf{B}$, and the volume susceptibility χ was taken as $800 \text{ kAm}^{-1} \text{ T}^{-1}$, suitable for commercial SPBs [54].

The relaxed magnetization configurations after saturating the film along $\theta = 0^\circ$ and $\theta = 45^\circ$ with respect to the x -axis (principal direction) are represented in Fig. 4(a) and (b) respectively. Fig. 4(c) and (d) also show the energy surface for $4.3 \mu\text{m}$ SPBs on the antidot array, without applying a magnetic field, for both the $\theta = 0^\circ$ and $\theta = 45^\circ$ cases, respectively. The direction θ of H_{IP} causes different remnant magnetic states, and the different states have a

significant influence on the magnetostatic potential energy landscape. In the $\theta = 0^\circ$ case, the potential wells are much deeper than in the $\theta = 45^\circ$ case, and the magnetic force in the $\theta = 0^\circ$ case is likewise expected to be greater than in the $\theta = 45^\circ$ case.

Fig. 5(a) and (b) show several cross-sections of potential wells for $4.3 \mu\text{m}$ SPBs at two different magnetic field conditions: the red area and the blue area in Fig. 3(b). The SPBs are located at the minimum position of the potential well, where the magnetic force vanishes and hence the bead is at an equilibrium position. The tracking of the two minimum positions differs. In Fig. 5(a), the minimum position is slowly moving to the right, but the position is hard to determine between 180° and 215° and it is divergent. This phenomenon is different from that in Fig. 5(b), in which the positions continuously move to the right. These graphs clearly show two different types of bead movements: transportation and oscillation. In addition, the magnetostatic potential well in Fig. 5(a) is shallow and it is insufficient to support the transport of SPBs when the magnetic field is below the threshold value. Otherwise, the magnetostatic potential well is deep and can provide the large magnetic force needed to move SPBs in the magnetic field that is described in Fig. 5(b). Thus, these graphs show why there are thresholds in the magnetic field.

Fig. 6(a)–(c) represent the relaxed magnetic configuration of a hexagonal anti-dot array and magnetostatic potential wells

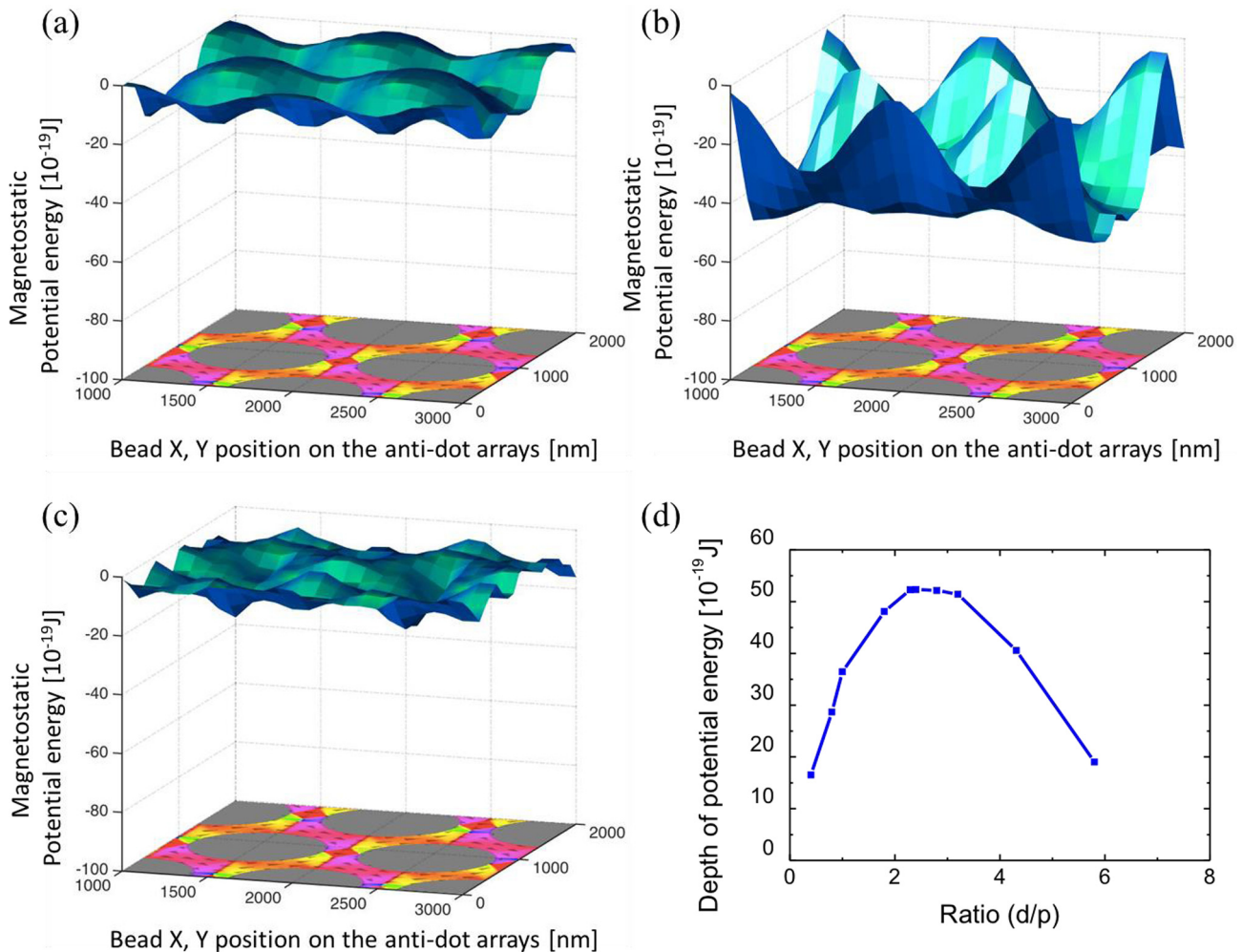


Fig. 6. The relaxed magnetization configuration and magnetostatic potential well at (a) $d/p = 0.4$, (b) $d/p = 2.4$, and (c) $d/p = 5.8$. (d) The depth of the magnetostatic potential well as a function of the diameter to periodicity ratio (d/p).

computed for several values of the ratio d/p of bead diameter to center-to-center spacing of the antidot lattice. Calculations are shown for d/p values of 0.4, 2.4, and 5.8. The shape of the potential well depends on the ratio, and the depth of potential well is shallow at both the low ratio and the high ratio limits. Fig. 6(d) shows the depth of the magnetostatic potential well as a function of d/p . At low ratio regime, where the period of the antidot array is larger than the diameter of SPBs, the magnetic force acting on the SPBs gradually strengthens as the diameter of SPBs increases up to a maximum, and then decreases with further increase in d/p . This can be understood in the limits: at small bead diameter, the magnetic potential decreases rapidly with bead volume. However, as the bead diameter becomes much larger than the feature size on the substrate, stray fields from adjacent holes are integrated over the bead volume, “smearing” out the potential. The numerical results suggest the existence of an optimum ratio for d/p , in the present case corresponding to ~ 2.4 .

Based on the observation that the critical field thresholds depend on bead size, one can use this phenomenon as a means to sort multi-bead mixtures of monodisperse beads with different sizes using an appropriately chosen rotating field. Fig. 7 shows sequential snapshots taken every 2 s on the square antidot array shown in Fig. 1(b) in the case of a rotating field applied in the xz plane. Here, a mixture of 2.8 μm and 4.3 μm diameter SPBs was placed on the substrate, and the field amplitudes were chosen to be intermediate between the transport thresholds for

these two bead sizes. The frequency of the driving field is about 1 Hz, and it is below the f_c of both sizes of SPBs. When the magnetic field is applied at a specific value that is higher than the threshold H_{IP} for 4.3 μm (circles) and lower than that for 2.8 μm , we can see that 4.3 μm SPBs are transported, whereas SPBs 2.8 μm simply oscillated back and forth. This demonstrates that the SPBs can be sorted through their own threshold values in the magnetic field.

Finally, we show that a simple, inexpensive large-area patterning can be achieved using self-assembled microsphere lithography to prepare antidot arrays that can be used for bead transport and separation. Fig. 8 shows a scanning electron micrograph of a 40 nm-thick Co layer patterned into a hexagonal antidot array with $p = 1 \mu\text{m}$ and hole size of $\sim 0.8 \mu\text{m}$. This pattern was formed by microsphere lithography, where monolayer ordered arrays of polystyrene microspheres were used as a lithography template. The diameter of polystyrene particles is 1 μm and reactive ion etching was conducted to tailor spacing sizes before depositing the thin-film over layers [55–61].

Fig. 8 shows that bead transport and size-based separation can be achieved reliably on this substrate, where we examine the rotating-field-driven motion of 2.8 μm and 5.8 μm beads. As anticipated from the simulations summarized in Fig. 6(d), we find similar critical frequency and field behavior in the transport behaviors for the large d/p limit that is applicable for the experimental case examined here. As in the previous cases examined above, f_c and threshold values in both H_{OOP} and H_{IP} depend on the size of SPBs d . To examine the d dependence on the threshold, we performed similar experiments as above to identify the field thresholds and critical frequencies. As shown in Fig. 8(b), f_c is located around 1.5 Hz and 2.5 Hz for 2.8 μm and 5.8 μm , respectively. In the case of H_{OOP} , the thresholds are found to be 1.1 mT and 0.8 mT for 2.8 μm , and 5.8 μm , respectively. Thus, the f_c as well as the threshold of the H_{OOP} can be used for selective transport of one subpopulation of SPBs. Fig. 8(c) shows snapshots during bead transport, in which size-based sorting on the microsphere lithograph-patterned substrate is achieved by tuning H_{OOP} to a value intermediate between the thresholds for the two bead sizes. As is evident in the images, the larger 5.8 μm beads can be transported reliably along the x direction while the smaller beads remain stationary.

4. Conclusions

In summary, we have studied the motion of fluid-suspended SPBs across a well-ordered magnetic structure consisting of periodic two-dimensional lattices of holes in a magnetic film. Our experiments have revealed critical frequencies and related threshold values in both H_{IP} and H_{OOP} . We determined that these thresholds are related to the depth of magnetostatic potential and find a dependence on bead size and substrate periodicity, and have explored these parameters experimentally and through modeling. Finally, we demonstrated that these parameters have different values according to the magnetized direction, the symmetry of pattern, and the diameter of the SPBs and that they can be used for the SPB separation in multi-bead populations. The possibility to design large-area patterned films using not only conventional optical lithography but also self-assembled microsphere lithography, opens up the possibility for inexpensive magnetically-textured landscapes that can be integrated over large-area lab-on-a-chip device. In addition, these results suggest further possibilities for more sophisticated directed sorting, in which anisotropic transport such as differing thresholds along different directions in a periodically-patterned structure might be used in conjunction with appropriate periodic driving fields to preferentially direct different

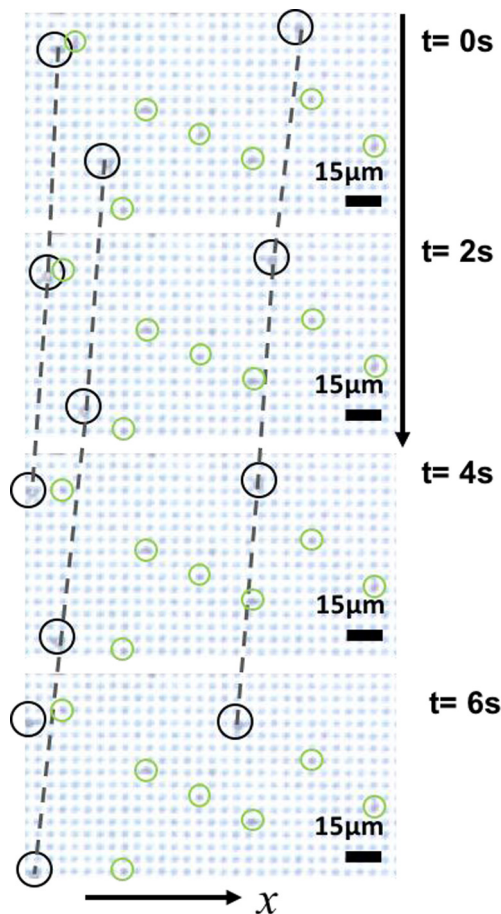


Fig. 7. Optical microscopy images showing a series of SPB movement snapshots taken every 2 s with 2.8 μm beads indicated as green circles and 4.3 μm beads as black circles when the field ($H_{IP} = 1.2 \text{ mT}$ and $H_{OOP} = 2.7 \text{ mT}$) is rotating counter-clockwise at 1 Hz. (For interpretation of the references to colour in this figure legend, the reader is referred to the web version of this article.)

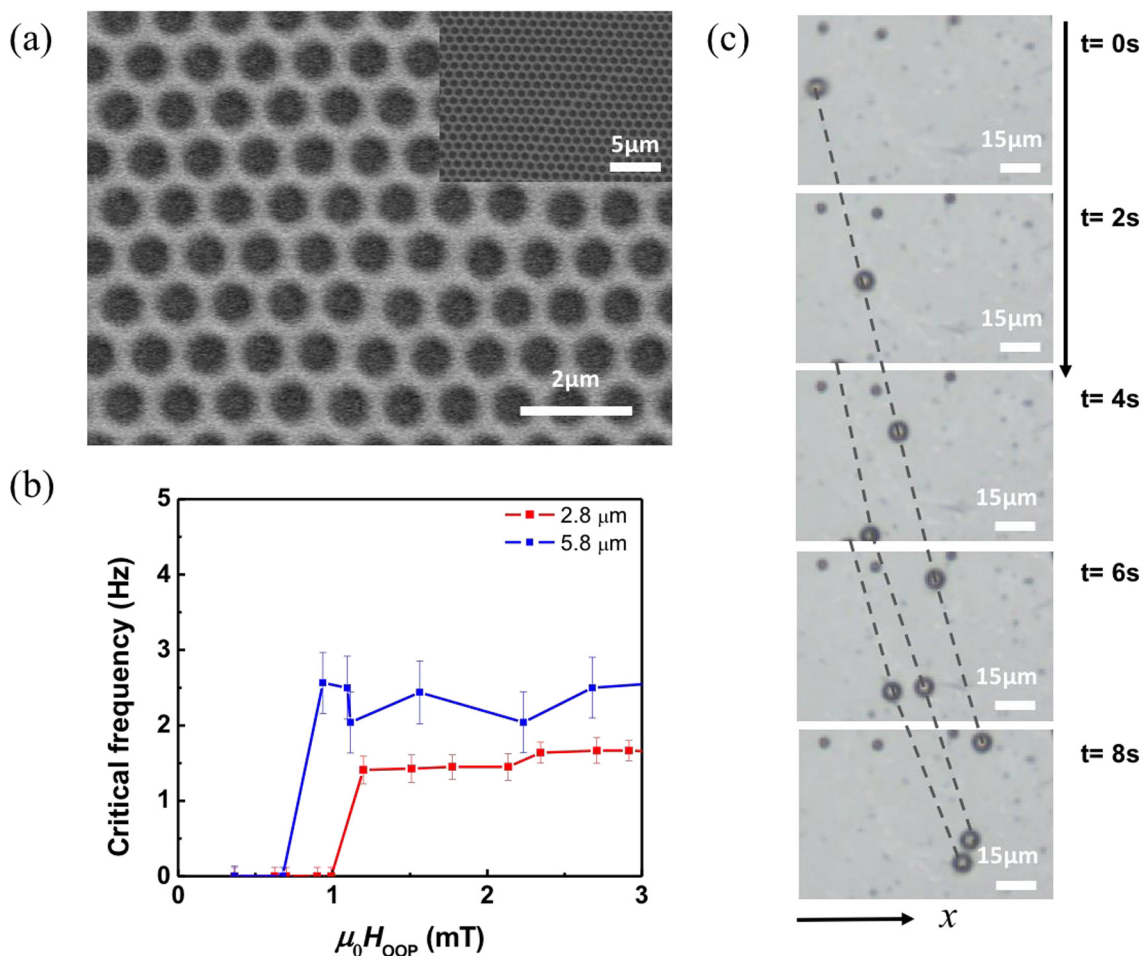


Fig. 8. (a) Scanning electron micrograph for a Co anti-dot arrays fabricated through microsphere lithography. The average diameter of the periodic anti-dot array is $\sim 0.8 \mu\text{m}$ and periodicity of array was $1 \mu\text{m}$. (b) The critical frequency as a function of H_{OOP} at $H_{IP} = 4.84 \text{ mT}$ with $2.8 \mu\text{m}$ and $5.8 \mu\text{m}$ of SPBs. (c) Series of optical microscopy images of SPB movement showing snapshots acquired every 2 s with $2.8 \mu\text{m}$ beads and $5.8 \mu\text{m}$ beads when the rotating magnetic field ($H_{IP} = 4.84 \text{ mT}$ and $H_{OOP} = 0.9 \text{ mT}$) in the clockwise direction at 1 Hz. We note that the microscope resolution does not permit the antidot structure of the patterned substrate to be seen in the images in panel (c).

beads along different directions, which is a topic for future research.

Acknowledgements

We gratefully acknowledge the computational support of A. Alexander-Katz and the assistance of Karim Gadelrab. M. Ouk acknowledges support from the Kwanjeong Fellowship Foundation.

Appendix A. Supplementary data

Supplementary data associated with this article can be found, in the online version, at <http://dx.doi.org/10.1016/j.jmmm.2017.07.096>.

References

- [1] Q.A. Pankhurst, J. Connolly, S.K. Jones, J. Dobson, Applications of magnetic nanoparticles in biomedicine, *J. Phys. D Appl. Phys.* 36 (2003) R167–R181.
- [2] M.A.M. Gijs, Magnetic bead handling on-chip: new opportunities for analytical applications, *Microfluid. Nanofluid.* 1 (2004) 22–40.
- [3] T. Neuberger, B. Schöpf, H. Hofmann, M. Hofmann, B. Von Rechenberg, Superparamagnetic nanoparticles for biomedical applications: possibilities and limitations of a new drug delivery system, *J. Magn. Magn. Mater.* 293 (2005) 483–496.
- [4] C. Fields, P. Li, J.J. O'Mahony, G.U. Lee, Advances in affinity ligand-functionalized nanomaterials for biomagnetic separation, *Biotechnol. Bioeng.* 113 (2016) 11–25.
- [5] L.R. Moore, M. Zborowski, L. Sun, J.J. Chalmers, Lymphocyte fractionation using immunomagnetic colloid and a dipole magnet flow cell sorter, *J. Biochem. Biophys. Meth.* 37 (1998) 11–33.
- [6] N. Pamme, C. Wilhelm, Continuous sorting of magnetic cells via on-chip free-flow magnetophoresis, *Lab Chip* 6 (2006) 974–980.
- [7] O. Lara, X. Tong, M. Zborowski, J.J. Chalmers, O. Lara, X. Tong, X. Tong, M. Zborowski, M. Zborowski, J.J. Chalmers, J.J. Chalmers, Enrichment of rare cancer cells through depletion of normal cells using density and ow-through, immunomagnetic cell separation, *Exp. Hematol.* 32 (2004) 891–904.
- [8] K. Smistrup, O. Hansen, H. Bruus, M.F. Hansen, Magnetic separation in microfluidic systems using microfabricated electromagnets - experiments and simulations, *J. Magn. Magn. Mater.* 293 (2005) 597–604.
- [9] Q. Ramadan, C. Yu, V. Samper, D.P. Poenar, Microcoils for transport of magnetic beads, *Appl. Phys. Lett.* 88 (2006) 1–3.
- [10] A. Rida, M.A.M. Gijs, Dynamics of magnetically retained supraparticle structures in a liquid flow, *Appl. Phys. Lett.* 85 (2004) 4986–4988.
- [11] D. Robert, N. Pamme, H. Conjeaud, F. Gazeau, A. Iles, C. Wilhelm, Cell sorting by endocytotic capacity in a microfluidic magnetophoresis device, *Lab Chip* 11 (2011) 1902–1910.
- [12] T.P. Forbes, S.P. Forry, Microfluidic magnetophoretic separations of immunomagnetically labeled rare mammalian cells, *Lab Chip* 12 (2012) 1471–1479.
- [13] P.S. Williams, M. Zborowski, J.J. Chalmers, Flow rate optimization for the quadrupole magnetic cell sorter, *Anal. Chem.* 71 (1999) 3799–3807.
- [14] Q. Ramadan, V. Samper, D. Poenar, C. Yu, On-chip micro-electromagnets for magnetic-based bio-molecules separation, *J. Magn. Magn. Mater.* 281 (2004) 150–172.
- [15] P. Tierno, F. Sagües, T.H. Johansen, T.M. Fischer, F. Sagües, T.H. Johansen, T.M. Fischer, T.H. Johansen, T.M. Fischer, Colloidal transport on magnetic garnet films, *Phys. Chem. Chem. Phys.* 11 (2009) 9615–9625.

- [16] K. Gunnarsson, P.E. Roy, S. Felton, J. Pihl, P. Svedlindh, S. Berner, H. Lidbaum, S. Oscarsson, Programmable motion and separation of single magnetic particles on patterned magnetic surfaces, *Adv. Mater.* 17 (2005) 1730–1734.
- [17] R.S. Conroy, G. Zabow, J. Moreland, A.P. Koretsky, Controlled transport of magnetic particles using soft magnetic patterns, *Appl. Phys. Lett.* 93 (2008).
- [18] B. Lim, I. Jeong, A. Sarella, K.W. Kim, C.G. Kim, Programmable magnetic actuation of biomolecule carriers using NiFe stepping stones, *J. Magn.* 16 (2011) 363–367.
- [19] P. Tierno, T.H. Johansen, T.M. Fischer, Fast and rewritable colloidal assembly via field synchronized particle swapping, *Appl. Phys. Lett.* 104 (2014).
- [20] P. Tierno, S.V. Reddy, Y. Jing, T.H. Johansen, T.M. Fischer, Transport of loaded and unloaded microcarriers in a colloidal magnetic shift register, *J. Phys. Chem. B* 111 (2007) 13479–13482.
- [21] E. Rapoport, G.S.D. Beach, Magneto-mechanical resonance of a single superparamagnetic microbead trapped by a magnetic domain wall, *J. Appl. Phys.* 111 (2012) 21–23.
- [22] E. Rapoport, D. Montana, G.S.D. Beach, Integrated capture, transport, and magneto-mechanical resonant sensing of superparamagnetic microbeads using magnetic domain walls, *Lab Chip* 12 (2012) 4433–4440.
- [23] E. Rapoport, G.S.D. Beach, Transport dynamics of superparamagnetic microbeads trapped by mobile magnetic domain walls, *Phys. Rev. B - Condens. Matter Mater. Phys.* 87 (2013) 21–24.
- [24] M. Donolato, P. Vavassori, M. Gobbi, M. Deryabina, M.F. Hansen, V. Metlushko, B. Ilic, M. Cantoni, D. Petti, S. Brivio, R. Bertacco, On-chip manipulation of protein-coated magnetic beads via domain-wall conduits, *Adv. Mater.* 22 (2010) 2706–2710.
- [25] M. Donolato, A. Torti, N. Kotesha, M. Deryabina, E. Sogne, P. Vavassori, M.F. Hansen, R. Bertacco, Magnetic domain wall conduits for single cell applications, *Lab Chip* 11 (2011) 2976–2983.
- [26] M. Donolato, F. Lofink, S. Hankemeier, J.M. Porro, H.P. Oepen, P. Vavassori, Characterization of domain wall-based traps for magnetic beads separation, *J. Appl. Phys.* 111 (2012) 07B336.
- [27] A. Chen, G. Vieira, T. Henighan, M. Howdyshe, J.A. North, A.J. Hauser, F.Y. Yang, M.G. Poirier, C. Jayaprakash, R. Sooryakumar, Regulating Brownian fluctuations with tunable microscopic magnetic traps, *Phys. Rev. Lett.* 107 (2011) 1–4.
- [28] M.T. Bryan, K.H. Smith, M.E. Real, M.A. Bashir, P.W. Fry, P. Fischer, M.Y. Im, T. Schrefl, D.A. Allwood, J.W. Haycock, Switchable cell trapping using superparamagnetic beads, *IEEE Magn. Lett.* 1 (2010) 3–6.
- [29] A. Sarella, A. Torti, M. Donolato, M. Pancaldi, P. Vavassori, Two-dimensional programmable manipulation of magnetic nanoparticles on-chip, *Adv. Mater.* 26 (2014) 2384–2390.
- [30] B.B. Yellen, R.M. Erb, H.S. Son, R. Hewlin Jr., H. Shang, G.U. Lee, Traveling wave magnetophoresis for high resolution chip based separations, *Lab Chip* 7 (2007) 1681–1688.
- [31] L. Gao, N.J. Gottron, L.N. Virgin, B.B. Yellen, The synchronization of superparamagnetic beads driven by a micro-magnetic ratchet, *Lab Chip* 10 (2010) 2108–2114.
- [32] L. Gao, M.A. Tahir, L.N. Virgin, B.B. Yellen, Multiplexing superparamagnetic beads driven by multi-frequency ratchets, *Lab Chip* 11 (2011) 4214–4220.
- [33] B.B. Yellen, L.N. Virgin, Nonlinear dynamics of superparamagnetic beads in a traveling magnetic-field wave, *Phys. Rev. E - Stat. Nonlinear Soft Matter Phys.* 80 (2009) 1–6.
- [34] M. Donolato, B.T. Dalslet, M.F. Hansen, Microstripes for transport and separation of magnetic particles, *Biomicrofluidics* 6 (2012).
- [35] A. Sarella, V.S. Rani, S. Oh, B.L. Sinha, M. Takahashi, C. Kim, Translocation of bio-functionalized magnetic beads using smart magnetophoresis, *Biosens. Bioelectron.* 26 (2010) 1755–1758.
- [36] A. Sarella, V. Sudha Rani, J.R. Jeong, C. Kim, K.W. Kim, B.P. Rao, Translocation of magnetic beads using patterned magnetic pathways for biosensing applications, *J. Appl. Phys.* 105 (2009) 2–4.
- [37] N.G. Deshpande, M.S. Seo, X.R. Jin, S.J. Lee, Y.P. Lee, J.Y. Rhee, K.W. Kim, Tailoring of magnetic properties of patterned cobalt antidots by simple manipulation of lattice symmetry, *Appl. Phys. Lett.* 96 (2010).
- [38] A. Manzin, O. Bottauscio, Micromagnetic modelling of the anisotropy properties of permalloy antidot arrays with hexagonal symmetry, *J. Phys. D. Appl. Phys.* 45 (2012) 95001.
- [39] Y.G. Ma, S.L. Lim, C.K. Ong, Evolution of magnetic and transport properties in pore-modified CoAlO antidot arrays, *J. Phys. D. Appl. Phys.* 40 (2007) 935–941.
- [40] S. Tacchi, M. Madami, G. Gubbiotti, G. Carlotti, A.O. Adeyeye, S. Neusser, B. Botters, D. Grundler, Angular dependence of magnetic normal modes in NiFe antidot lattices with different lattice symmetry, *IEEE Trans. Magn.* 46 (2010) 1440–1443.
- [41] P. Vavassori, G. Gubbiotti, G. Zangari, C.T. Yu, H. Yin, H. Jiang, G.J. Mankey, Lattice symmetry and magnetization reversal in micron-size antidot arrays in Permalloy film, *J. Appl. Phys.* 91 (2002) 7992–7994.
- [42] C.C. Wang, A.O. Adeyeye, N. Singh, Magnetic antidot nanostructures: effect of lattice geometry, *Nanotechnology* 17 (2006) 1629.
- [43] M. Melzer, D. Makarow, A. Calvimontes, D. Karnaushenko, S. Baunack, R. Kaltfen, Y. Mei, O.G. Schmidt, Stretchable magnetoelectronics, *Nano Lett.* 11 (2011) 2522–2526.
- [44] M. Donolato, C. Tollan, J.M. Porro, A. Berger, P. Vavassori, Flexible and stretchable polymers with embedded magnetic nanostructures, *Adv. Mater.* 25 (2013) 623–629.
- [45] M. Grimsditch, Y. Jaccard, I.K. Schuller, Magnetic anisotropies in dot arrays: shape anisotropy versus coupling, *Phys. Rev. B* 58 (1998) 539–543.
- [46] L.E. Helseth, T.M. Fischer, R.W. Hansen, T.H. Johansen, Microscopic magnetic squeezer, *Appl. Phys. Lett.* 85 (2004) 2556–2558.
- [47] S.S. Shevkopyas, A.C. Siegel, R.M. Westervelt, M.G. Prentiss, G.M. Whitesides, The force acting on a superparamagnetic bead due to an applied magnetic field, *Lab Chip* 7 (2007) 1294–1302.
- [48] P. Tierno, R. Golestanian, I. Pagonabarraga, F. Sagues, Controlled swimming in confined fluids of magnetically actuated colloidal rotors, *Phys. Rev. Lett.* 101 (2008) 218304–218311.
- [49] H. Morimoto, T. Ukai, Y. Nagaoka, N. Grobert, T. Maekawa, Tumbling motion of magnetic particles on a magnetic substrate induced by a rotational magnetic field, *Phys. Rev. E - Stat. Nonlinear Soft Matter Phys.* 78 (2008), 021403–1.
- [50] C.E. Sing, L. Schmid, M.F. Schneider, T. Franke, A. Alexander-Katz, Controlled surface-induced flows from the motion of self-assembled colloidal walkers, *Proc. Natl. Acad. Sci. U.S.A.* 107 (2010) 535–540.
- [51] A.W. Mahoney, J.J. Abbott, Managing magnetic force applied to a magnetic device by a rotating dipole field, *Appl. Phys. Lett.* 99 (2011) 134103–134111.
- [52] K.E. Peyer, B.J. Nelson, Bio-inspired magnetic swimming microrobots for biomedical applications, *Nanoscale* 5 (2013) 1259–1272.
- [53] A. Vansteenkiste, B. Van De Wiele, MUMAX: a new high-performance micromagnetic simulation tool, *J. Magn. Magn. Mater.* 323 (2011) 2585–2591.
- [54] R.J.S. Derks, A. Dietzel, R. Wimberger-Friedl, M.W.J. Prins, Magnetic bead manipulation in a sub-microliter fluid volume applicable for biosensing, *Microfluid. Nanofluid.* 3 (2007) 141–149.
- [55] J.C. Hulst, Nanosphere lithography: a materials general fabrication process for periodic particle array surfaces, *J. Vac. Sci. Technol. A Vac. Surf. Film* 13 (1995) 1553.
- [56] A.A. Zhukov, A.V. Goncharov, P.A.J. de Groot, P.N. Bartlett, M.A. Ghanem, Magnetic antidot arrays from self-assembly template methods, *J. Appl. Phys.* 93 (2003) 7322–7324.
- [57] C.C. Ho, T.W. Hsieh, H.H. Kung, W.T. Juan, K.H. Lin, W.L. Lee, Reduced saturation magnetization in cobalt antidot thin films prepared by polyethylene oxide-assisted self-assembly of polystyrene nanospheres, *Appl. Phys. Lett.* 96 (2010) 3–5.
- [58] J. Kim, J. Kim, S.G. Cho, Y.H. Choa, G.J. Shin, Microstructures and the corresponding magnetic properties of antidot arrays, *Thin Solid Films* 520 (2012) 3013–3016.
- [59] X. Ye, L. Qi, Two-dimensionally patterned nanostructures based on monolayer colloidal crystals: controllable fabrication, assembly, and applications, *Nano Today* 6 (2011) 608–631.
- [60] F. Burmeister, C. Schäfle, T. Matthes, M. Böhmisch, J. Boneberg, P. Leiderer, Colloid monolayers as versatile lithographic masks, *Langmuir* 13 (1997) 2983–2987.
- [61] C.L. Haynes, R.P. Van Duyne, Nanosphere lithography: a versatile nanofabrication tool for studies of size-dependent nanoparticle optics, *J. Phys. Chem. B* 105 (2001) 5599–5611.